Wear 378-379 (2017) 136–144

Contents lists available at ScienceDirect

Wear

journal homepage: www.elsevier.com/locate/wear

# Effect of polymer interlayer on scratch resistance of hard film: Experiments and finite element modeling

C.H. Sacré [a,b,*], F. Lani [a], Ph. Guaino [b], L. Libralesso [b], A. Favache [a], T. Pardoen [a]

[a] Institute of Mechanics, Materials and Civil Engineering, Université catholique de Louvain, Place Sainte Barbe 2 L5.02.02, 1348 Louvain-la-Neuve, Belgium
[b] Advanced Coatings and Construction Solutions - CRM Group, Allée de l'Innovation 1, Quartier Polytech 3, 4000 Liege, Belgium

ARTICLE INFO

*Article history:*
Received 16 June 2016
Received in revised form
13 January 2017
Accepted 10 February 2017
Available online 14 February 2017

*Keywords:*
Nanoscratch
Thin films
Oxide
Fracture
Polymer
FEM

ABSTRACT

The scratch resistance of thin ZnO films deposited on a polyimide interlayer is characterized experimentally and simulated using a 3D finite element model. Nanoscratch tests combined with scanning electron microscopy observation to analyze the failure mechanisms in the brittle hard films are performed. The thickness of the polymer interlayer is shown to play a major role in controlling the scratch depth and the initiation of the cracks in the top hard coating. The main feature dictating the scratch resistance is related to the development of the pile-up in front of the indentation tip. The amplitude and morphology of the pile-up is affected by the polymer constitutive behaviour and by the constraint induced by the limited thickness. The finite element simulations accurately capture the changes in pile-up development with different soft interlayer thicknesses as well as, based on a simple maximum principal stress criterion, the onset of the cracking process.



## 1. Introduction

Advanced coatings composed of ultra-thin metallic or ceramic hard films deposited on a polymer interlayer have been developed to meet multifunctional requirements including electrical and bio-chemical performances, corrosion resistance or aesthetic properties [1,2]. In these applications, the motivation for introducing a polymer interlayer is to smooth the roughness, to provide corrosion resistance and/or to allow electrical insulation [3]. The hard layer itself meets the scratch resistance, electrical conductivity or semi-conductor function in the case of electronic devices. Multi-layered systems are extensively used in microelectronic applications such as bio-compatible stretchable devices [4], OLEDs and photovoltaic systems [5,6].

In current and future developments, these systems, schematically represented in Fig. 1, must reconcile functional performances with proper tribological behavior, in particular, for many applications, good scratch resistance. The objective of this work is to unravel the mechanisms that control the scratch resistance as a function of the film characteristics as well as of the polymer interlayer mechanical response and thickness. A central issue is the identification of the predominant damage mechanisms occurring during sliding contact in the present case of a thin hard film deposited on a soft interlayer involving thus a high modulus mismatch.

Researches on the mechanics of hard films on polymers have mainly focused on the tensile and bending resistance, involving, for instance, Au films on PET or polyimide, e.g. [7–9]. Only very few studies have addressed tribological aspects involving nanoindentation [10,11] or nanoscratch [12,13]. The complexity of the stress and strain distribution in bi- and tri-layer systems with these types of loadings requires to use finite element modelling (FEM) to quantitatively understand the system behavior.

Nanoindentation of bilayer systems has been widely studied in the literature, but focusing merely on the error due to the substrate effect in the extraction of the Young's modulus and hardness [14,15]. A. Pelegri [10] looked at the load transfer/substrate interactions during nanoindentation as well as on the importance of properly studying the pile-up and the sink-in during indentation. Cracking of thin brittle films on soft substrates under indentation load has been considered in some studies [16–19,11].

Earlier studies on scratch have identified the failure mechanisms on bulk materials, leading to the classification of the critical damage phenomena [20,21] in terms of wear maps and tables. The mechanisms involve different elastic, plastic and cracking dominated patterns with varying morphologies and amplitudes which depend on the intrinsic stiffness, hardness, fracture toughness and adhesion of the layers. These studies lead to wear maps and reference tables aimed at predicting fatal failure in material subjected to contact solicitations. Beside these more phenomenological analyses, scratch induced stress and strain distributions in

* Corresponding author at: Institute of Mechanics, Materials and Civil Engineering, Université catholique de Louvain, Place Sainte Barbe 2 L5.02.02, 1348 Louvain-la-Neuve, Belgium.

http://dx.doi.org/10.1016/j.wear.2017.02.033
0043-1648/

**Nomenclature**

*Index*

| | |
|---|---|
| $t_f$ | thickness of the film |
| $t_p$ | thickness of the polymer |
| $E_f$ | modulus of the film |
| $E_p$ | modulus of the polymer |
| $\nu_f$ | Poisson ratio of the film |
| $\nu_p$ | Poisson ratio of the polymer |
| $\delta_z$ | displacement normal to the surface |

bulk materials have been considered in several in depth studies [22–24]. Special attention with respect to pile-up formation was paid in [25]. Using a "microvisioscratch" method and FEM, J.L. Bucaille and C. Gauthier demonstrated the strong dependency of the elastic recovery and pile-up formation on the strain hardening behavior of the polymer [26]. The case of scratching in bilayers has been studied by FEM for instance in [27] (hard thin film on elastoplastic substrate) and in [28](soft layer on hard and soft substrates).

In the latter study, the stress distribution between the coating and the substrate in the case of a soft substrate is shown to be a key element to reduce scratch damages. Let us notice that in the previously cited studies, the problem configuration is a bilayer, mostly either a hard film on a bulk soft layer or a soft layer on a harder substrate. The case of a geometrically confined thick polymer layer sandwiched between a hard brittle thin coating and a hard substrate has not been addressed, although a significant number of applications show this configuration (e.g. organic photovoltaic cells on glass substrates, micro-electro-mechanic systems). As it has already been highlighted in [12] and will be more deeply analyzed in the present paper, this configuration is a combination of the case of a hard brittle thin film on a soft layer with respect to film cracking and of a soft layer on a hard substrate with respect to the deformation. Indeed, this recent study by our team focused on fracture mechanics analysis of brittle chromium nitride films on a polymer interlayer, insisting on the impact of the polymer thickness on the damage evolution. First tentative ideas towards an understanding of the experimental observations have been given. But the lack of more rigorous understanding on the scratch pattern and on the deformation induced by the tip was emphasized. Similarly, P. Chouwatat et al. experimentally observed that a thicker PMMA interlayer reduces the scratch damage compared to a thinner one in the case of acrylic coating [29]. However, the thickness and material properties ratios are much lower than in the case addressed here.

The general objective of this work is to characterize and to model the effect of a polymer interlayer on the scratch resistance of a top hard coatings. The system of interest is ZnO on polyimide. The ZnO film on polyimide system has been selected as a good reference case for applications in micro-electronics, photovoltaïcs

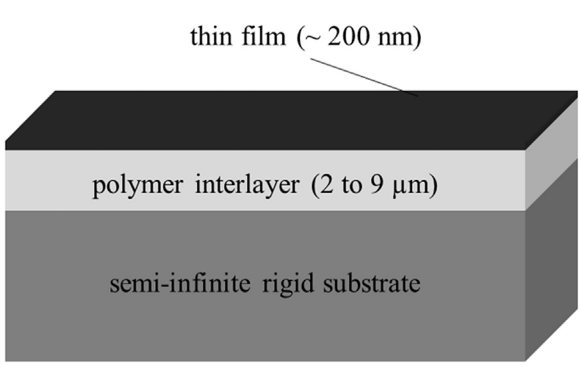


**Fig. 1.** Schematic representation of hard thin film deposited on polymer interlayer.

or sensor devices [30,31]. The choice of ZnO is also motivated for its potential as transparent layer for automotive paint protection [32]. Nevertheless, the results and analysis are certainly more general and have application to a wider range of hard films on soft interlayers. Section 3 describes the experimental results involving the (3.1) material properties, (3.2) the scratch resistance of the uncoated polymer on Si and (3.3) the scratch resistance of the coated polymer interlayer. The data presented in the experimental section are depicted and discussed using finite element modeling in Section 4.

## 2. Materials and methods

### 2.1. Processing of the coatings

Polyimide films were produced from a commercial precursor PI 2562 provided by HD Microsystems on 3 inches Si wafers with various thicknesses by a spin coating technique with prior application of the adhesion promoter VM652 from HD Microsystems. Some films have also been deposited onto stainless steel substrate. The same results and conclusion as the one reported in the present paper have been obtained. For the sake of conciseness, we will only present results obtained for Si substrate which involve the best conditions in terms of roughness. After precursor spincoating, the Si wafers were soft-baked at 100 °Cfor 2 minutes on a hot plate in order to evaporate most of the solvent. Finally, the coated wafers were cured under controlled atmosphere following these steps: heating at 4 °C/min from RT to 200 °C, holding at 200 °Cfor 30 min in air, heating at 2.5 °C/min from 200 °Cto 350 °Cin nitrogen, holding for 60 min in nitrogen and gradually cooling down to room temperature.

ZnO films were prepared by magnetron sputtering configuration in a Kurt J. Lesker CMS chamber from a 99.99997 % ZnO target from Neyco Company. The set of deposition parameters were the following: the substrate was kept at room temperature, the sputter R.F. power was equal to 250 W and the chamber pressure was equal to 13 µbar. ZnO films were deposited directly on the polyimide layer to form the bi-layered system "hard film/soft interlayer/substrate". For characterization purpose, some ZnO films were also deposited on a bare Si wafer without any polymer interlayer. A summary of the systems discussed in the paper is given in Table 1.

**Table 1**
Presentation of the different systems with thickness.

| Systems | Polyimide | $t_p$ | ZnO | $t_f$ |
|---|---|---|---|---|
| Bilayer | PI 2562 | $2.14 \pm 0.15$ µm | Sputtering | $200 \pm 10$ nm |
| Bilayer | PI 2562 | $4.58 \pm 0.05$ µm | Sputtering | $200 \pm 10$ nm |
| Bilayer | PI 2562 | $8.99 \pm 0.15$ µm | Sputtering | $200 \pm 10$ nm |
| Monolayer | PI 2562 | $1 \pm 0.20$ µm | | |
| Monolayer | | | Sputtering | $200 \pm 10$ nm |

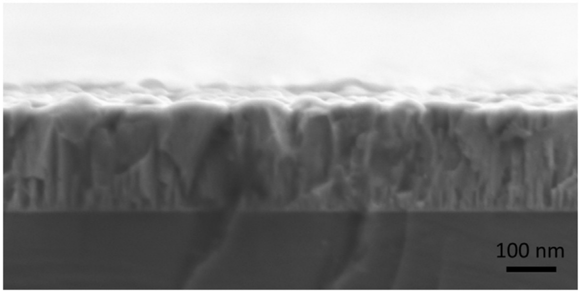


**Fig. 2.** Cross-section SEM micrograph of ZnO film on Si substrate.

### 2.2. Structural characterization

The ZnO film thickness has been measured after deposition using a mechanical profilometer while the polyimide film thickness was estimated through weight measurements after curing. Each sample is measured at 5 different positions over the Si wafer surface. The uniformity of the thickness has been checked on cross-sections by SEM. The thicknesses are reported in Table 1. XRD diffraction spectra indicate preferential (002) growth corresponding to the hexagonal wurzite structure of ZnO [33,34]. Cross-sectional SEM micrographs, shown in Fig. 2, exhibit a columnar morphology starting at the interface with a small-grained structure evolving into larger columnar grains.

The elastic modulus and hardness of the coatings were evaluated by nanoindentation with an Agilent Technology G200 nanoindenter. The mechanical properties have been evaluated using the Dynamic Contact Module II (DCM) with the Continuous Stiffness Measurement module (CSM). The CSM module allows the determination of the modulus and hardness as the tip penetrates the surface. The raw nanoindentation results have been analyzed using the standard Oliver and Pharr method [35], as presented in Section 3.1.

### 2.3. Scratch testing

Nanoscratch tests have been performed using the same Agilent G200 equipment with a XP head. The XP head provides a load range up to 500 mN. The Lateral Force Measurement (LFM) module allows continuous evaluation of the tangential force and hence of the friction coefficient as a function of the tip penetration into in the multilayer. A sphero-conical diamond tip of 5 µm equivalent radius and a 60 degrees cone equivalent angle is drown continuously and linearly into the sample to reach 20 mN after a maximum sliding distance of 100 µm at a speed of 30 µm.s$^{-1}$. The variation of the load is linear with the lateral displacement. The surface profile is scanned before and after scratching by displacing the scratch tip under very low normal forces ($F_{scan}$ = 20 µN). This pre-scratch scan provides an estimate of the surface roughness, defects, and possible sample curvature and tilt. After scratching, the tip is moved once again in the scratch groove under a very small force in order to extract the effective penetration depth after elastic recovery. In the following figures, the three steps are superposed for comparison purpose in the following order from bottom to top: scratching, post-scratch and pre-scratch. The scan length is 40 % longer than the scratch length in order to monitor the accumulation of material, pile-up, in front of the scratch tip. Each sample is scratched 4 times for reproducibility purposes. Scratch grooves are observed afterwards by SEM to characterize the damage and failure mechanisms.

**Table 2**
ZnO and polyimide mechanical properties measured by nanoindentation to support FEM analysis.

| Material | Elastic modulus | Hardness |
|---|---|---|
| ZnO | 100 ± 10 GPa | 8 ± 0.5 GPa |
| Polyimide | 6 ± 0.2 GPa | 0.18 ± 0.1 GPa |

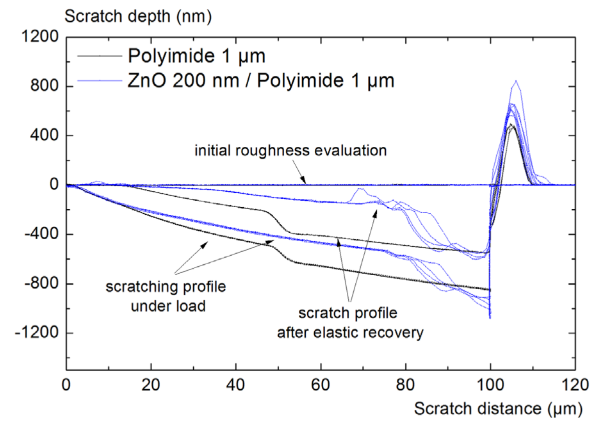


**Fig. 3.** Variation of the penetration depth as a function of the scratch distance (which is proportional to the applied normal load) on 1 µm thick polyimide and on a 200 nm thick ZnO on top of a 1 µm thick polyimide layer.

## 3. Experimental results

### 3.1. Main characteristics of the layers

The hardness and elastic modulus of ZnO films deposited on Si substrate are equal to 8 ± 0.5 and 100 ± 10 GPa, respectively.

The polyimide films have a hardness equal to 0.18 ± 0.1 GPa and an elastic modulus of 6 ± 0.2 GPa after curing. For comparison purposes, the hardness $H$ is translated into a yield stress $\sigma_y$ using Tabor's relationship $\sigma_y = H/3$. This yield stress value is an important data for the failure analysis by finite element modeling in Section 4. These values are summarized in Table 2.

### 3.2. Scratch resistance of coated versus un-coated polyimide

In order to understand the effect of an additional hard layer on a polymer on the global scratch resistance, two samples have been tested using instrumented nanoscratching. These samples consist of a 1 µm polyimide deposited on Si wafers with and without a ZnO top layer. The graph corresponding to the scratch response of both samples is given in Fig. 3. The curves corresponding to the uncoated polyimide show that the tip penetration during progressive loading reaches a maximum depth of 800 nm after 100 µm scratch distance (Eq. 20 mN applied normal load). At 50 µm scratch length (Eq. 10 mN applied normal force), the penetration depth suddenly increases. This feature is probably attributed to a plastic collapse mechanism occurring in the polymer but it has not been further investigated. When a 200 nm hard ZnO film is added on top of the 1 µm polyimide, the occurrence of failure is shifted to larger load values corresponding to roughly similar indentation depth. The corresponding load increases from 10 mN up to 15 mN. Beyond 80 µm scratch length, the tip breaks through the ZnO film and the polyimide collapses. The depth that is attained correlates well with the film thickness. The tip gets very close to the substrate interface without scratching it. The friction coefficient is estimated using lateral force measurement and is

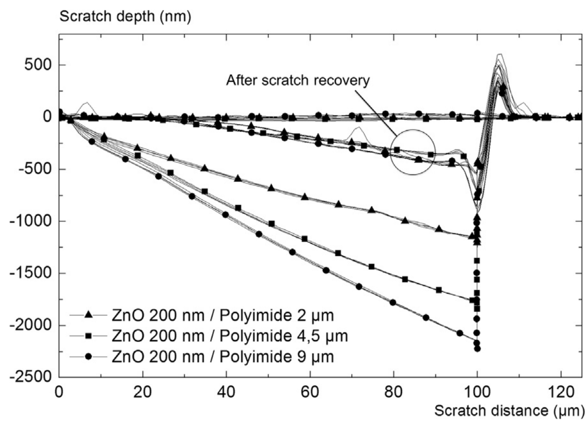


**Fig. 4.** Variation of the penetration depth as a function of scratch distance for samples with 200 nm thick ZnO on top of: 2 μm, 4.5 μm and 9 μm thick polymer interlayers.

equal to 0.1 ± 0.05 for ZnO coated systems. The failure mechanisms will be addressed in Section 3.3.2 and further discussed in Section 4 in light of the mechanical simulations.

### 3.3. Scratch resistance of coated polymer on Si

#### 3.3.1. Description of the scratch test results

Fig. 4 shows the evolution of the tip penetration depth with scratch distance into three different bi-layered systems during the scratch and after elastic recovery. These systems consist of 200 nm ZnO thin film deposited on 3 polyimide interlayer thicknesses on Si, 2 μm, 4.5 μm and 9 μm as reported in Table 1. For all conditions, the scratch depth increases with increasing load to reach a maximum at 100 μm scratch length. During the scratch, at very low applied forces (i.e. at the beginning of the scratch), the tip penetration profile is almost similar for all polyimide thicknesses. Soon after the penetration, the response differs with the polymer thickness due to substrate effect as explained already in [10] for normal indentation and in [12]. At shallow depth, the film response is comparable to bulk material in terms of load transfer but the substrate effect shows up very early in the process. At higher load, the curves split even more to reach markedly different penetration depths equal to 1200 ± 10 nm, 1850 ± 10 nm, and 2200 ± 15 nm for, respectively, the 2 μm, 4.5 μm and 9 μm polyimide interlayers. After 100 μm, the post scan reveals marked pile-up formation with a height between 200 nm and 500 nm. This pile-up is quantified in Section 3.3.3.

#### 3.3.2. Failure mechanisms

The scratch track has been characterized by Scanning Electron Microscopy (SEM) to determine at which distance from the beginning of the track cracks initiate and delamination takes place [27].

Fig. 5 shows micrographs of the scratch tracks produced in a 200 nm ZnO film deposited on *(a)* 2 μm, *(b)* 4.5 μm and *(c)* 9 μm polyimide interlayer. All micrographs have been taken at the end of the scratch test after the removal of the indentation tip. The end of the scratch zone for the 2 μm polyimide shows significant chipping of the ZnO layer. A large amount of ZnO flakes can be seen in the scratch track. The film is not continuous anymore. Several flakes sink into the polyimide interlayer. Polyimide appears with the highest contrast. A few flakes are ejected out of the scratch track along the edges and in front of the tip. The damage development in the 4.5 μm interlayer is much less obvious. At this intermediate thickness, flakes are mainly formed inside the scratch track, but the polymer cannot be seen beneath. In the 9 μm interlayer, cracks are barely visible.

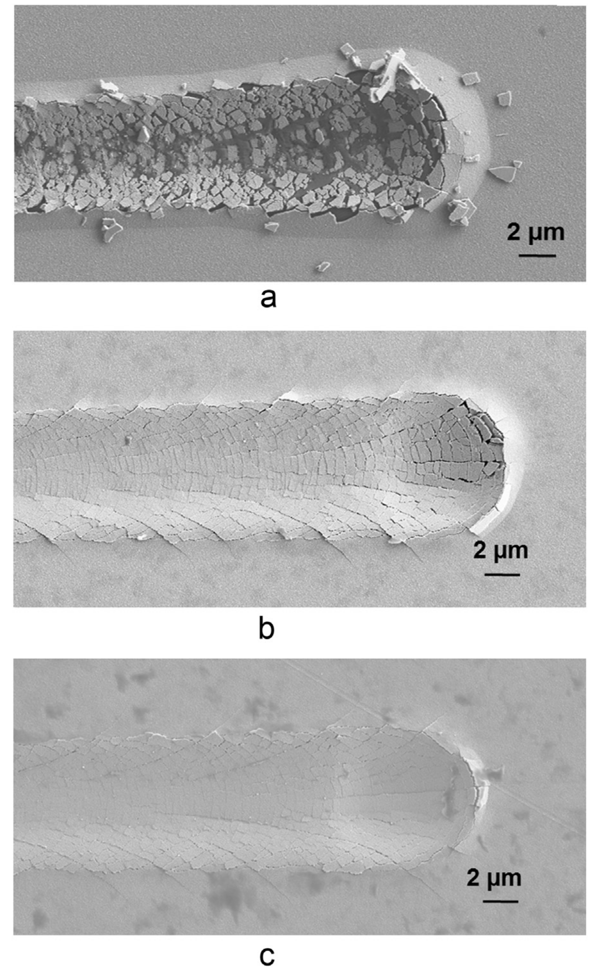


**Fig. 5.** SEM micrographs of nanoscratch tracks in 200 nm thick ZnO film deposited on (a) 2 μm polyimide, (b) 4.5 μm polyimide and (c) 9 μm polyimide films.

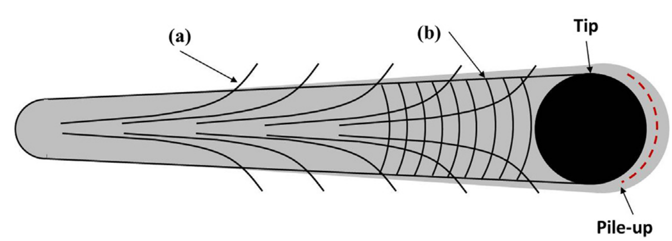


**Fig. 6.** Schematic representation of scratch grooves in coated systems with (a) in-track cracks and (b) transverse cracks.

Based on this observation, a schematic representation in Fig. 6 illustrates the morphology of the cracks. The first cracks to form, so called "in-track" cracks, start from the scratch track under the tip and propagate in the scratch direction until deviating out of the track at an angle close to 45°. The "in track" cracks do not seem to be critical for the integrity of the film, if we take, as failure criterion, the appearance of the underneath polymer. The second type of cracks, called "transverse cracks" in Fig. 6, propagates in the direction transverse to the track. These cracks have been observed by Bull [20] on several types of coatings who explains that conformal cracking forms at the front and along the side of the indenter. The interaction between the "in track" and "transverse cracks" leads to the formation of small isolated flakes. Increasing the load results in the implantation or detachment of the flakes. In

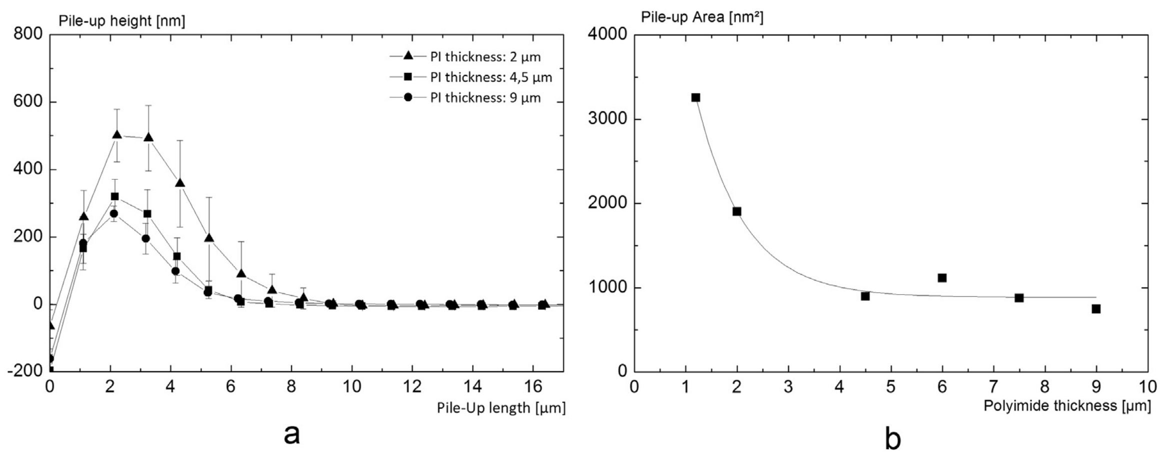


**Fig. 7.** (a) Pile-up elevation profile for three polyimide interlayer thicknesses: 2 µm, 4.5 µm, 9 µm (b) Variation of pile-up area with polyimide interlayer thickness.

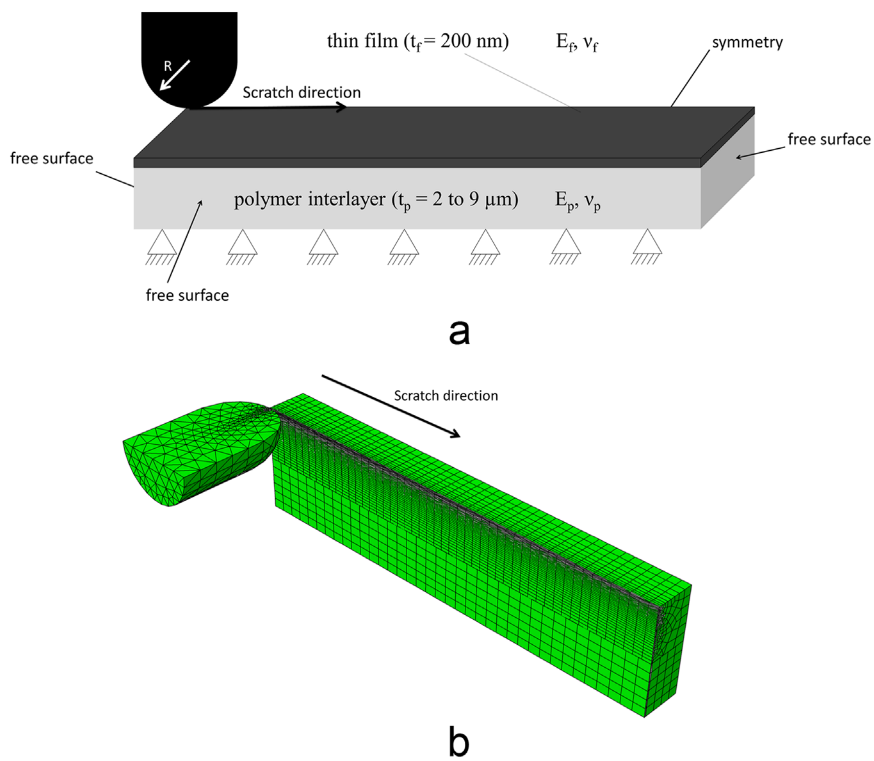


**Fig. 8.** (a) Schematic representation of the finite element model and (b) associated finite element mesh.

the 9 µm polyimide thickness system, even though the penetration of the tip is larger than for other systems, the surface is less damaged. The "in track" cracks dominate. The first major transverse crack can be observed when focusing on the front of the last tip position.

To summarize, the thicker polymer underlayer leads to the largest tip penetration (at equivalent load) but also to the less damaged surface. The scratch experiments at higher loads on the 4.5 µm and 9 µm polyimide thickness exhibit the same failure mechanisms as for the 2 µm polyimide thickness. There is thus a delaying effect associated to an increasing interlayer polymer thickness or, vice-versa, a reduction of the scratch resistance when decreasing the interlayer thickness, confirming earlier results on CrN films [12].

### 3.3.3. *Characterization of the pile-up*

As shown in Fig. 4 and depicted in Fig. 5, the pile-up which develops in front of the tip appears to be larger for the 2 µm polyimide thickness. The nanoscratch instrument allows a post scan of the scratch groove: Fig. 7 shows the pile-up height as a function of the distance from the end of the scratch. The height of the pile-up clearly decreases for increasing polyimide thickness. For the lowest polyimide thickness, the pile-up at the tip apex reaches $0.5 \pm 0.1$ µm, while for the 9 µm polyimide thickness, the pile-up height is only $0.28 \pm 0.02$ µm indicating a decrease by almost a factor of two. The same observation can be made for the width of the pile-up. The thinner is the polyimide, the wider the front pile-up.

Fig. 7 shows the variation of the "pile-up section area" for three different polyimide thicknesses ranging from 2 µm up to 9 µm. The pile-up section area is defined as the area under the curve. This variation of the pile-up section area as a function of the polyimide thickness shows a large decrease of the pile up amplitude as the underneath polyimide thickness increases.

The following working hypothesis can thus be made from this observation: a thinner polyimide is more geometrically confined between the ZnO coating and the substrate than a thicker one; this confinement creates a stronger pile-up. The bending of the ZnO layer on top of the pile-up can be large enough to lead to the tensile cracking of the hard film in front of the tip constituting the dominant critical mechanism for the integrity of the coating when subjected to scratch conditions. This hypothesis is further explored in the following section using more quantitative arguments.

## 4. Finite element model of the scratch and discussion

### 4.1. Description of the model

A finite element model of cono-spherical scratch of a hard film onto a polymer interlayer laying on a stiff substrate was setup using the commercial finite element software ABAQUS/Standard. The objective of the model is to quantify the stress and strain fields along and inside the scratch track, with a specific focus on the pile-up formation in order, among others, to unravel the origin of the interlayer thickness effect. The stress state at the top of the pile-up is of particular interest in order to establish a crack initiation condition. The focus is on the first large crack before delamination and chipping failure occurring from the top of the pile-up.

A fully parametric 3D model is created using the FE code, involving the tip radius and opening angle, the layer thicknesses and the associated material properties. Due to the specimen and loading symmetry, only one half of the specimen is modeled with symmetric boundary conditions applied along the scratch direction Fig. 8.

The bottom surface of the polymer is completely fixed considering the substrate as rigid. In order to keep the computational time within a reasonable range without losing the relevant information, only 50 µm, half of the total experimental length, is modeled. The loading scheme is equivalent to the experimental equal to 0.2 mN/ µm. Because of boundary effects we limit the analysis to 40 µm in order to avoid artifacts due to approaching the edge of the simulation domain. The model is meshed using 3D quadratic hexahedral elements C3D20R, C3D8R and C3D4. The simulation is divided in two steps: a first approaching step initiates the contact between the tip and the top layer, followed by the scratch step during which the load and the tangential displacement are imposed. The contact is obtained between the master tip surface and the slave sample surface with a friction value of 0.1 as experimentally measured by nanoscratch. The 5 µm tip radius is meshed using C3D15 elements. The indenter is considered as elastic following Hooke's law with a Young's modulus equal to 1141 GPa and Poisson ratio equal to 0.07 [35]. The ZnO layer is considered as purely elastic with the elastic modulus measured as equal to 100 GPa and a Poisson ratio equal to 0.25 [36]. The model does not account for the generation of the early appearing “in track” cracks shown in the micrographs of Figs. 5 and 6. The polyimide elastoplastic behavior is modeled with Hooke's law as long as the Von Mises stress is lower than the yield stress $\sigma_0$. The $J_2$ flow theory is used to model the plastic response using the following simple hardening law:

$$\sigma = \sigma_0 + k\epsilon^n \tag{1}$$

where $k$ is a material hardening coefficient and $n$ is the strain hardening exponent. The Young's modulus is taken as the experimentally determined value by nanoindentation equal to 6 GPa. The yield strength $\sigma_0$ is estimated using Tabor's law as one third of the hardness [37], i.e. $\sigma_0 = 62.5$ MPa, while $k$ and $n$ are respectively set equal to 217 MPa and 0.77 after fitting the stress-strain curve of polyimide [38].

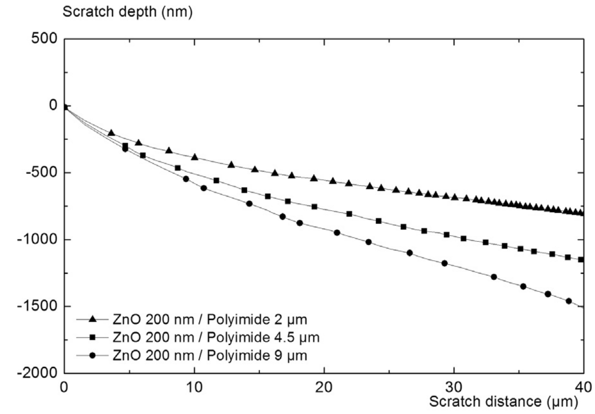


**Fig. 9.** Variation of the penetration depths under scratch loading as a function of the scratch distance as predicted by finite element simulations.

### 4.2. Force penetration prediction

The penetration depths, under loading, predicted by finite element simulations in Fig. 9 compare the experimental penetration profiles as already shown in Fig. 4.

The slight differences in penetration depths between the experimental and numerical results are attributed to the approximation used to represent the polymer mechanical behavior in the numerical model. The most important outcome is that the ordering of the final penetration is indeed respected that is to say for the same maximum applied load, the tip goes deeper as the polymer thickness increases as for the experiments.

### 4.3. Pile-up analysis

Fig. 10 (a) shows the iso-displacement, out of plane displacement, contours corresponding to a 200 nm ZnO layer deposited on 2 µm polyimide interlayer under scratch loading conditions. The tip is located at 36 µm from the starting point, corresponding to 7.2 mN applied load. In Fig. 10, a symmetry has been applied along the middle of the scratch in order to show a full scratch pattern from the top view. The area located under the tip and in the scratch groove involves a negative displacement corresponding to the tip penetration below the surface. The displacements are positive along the edges as well as in front of the tip. For 36 µm scratch length the pile-up is narrow with a height reaching 75 % of the film thickness. At similar scratch length – Fig. 10 (a) (b) and (c) –, the pile-up amplitude is lower for the 4.5 µm polyimide thickness (50 % of film thickness) and even lower for the 9 µm thickness (5 % of film thickness). Fig. 11 presents the normalized pile-up height coming from the numerical model compared to the experimental pile-up. The FEM profile is measured at 36 µm tip displacement under loading. Even with the simple hardening law used in the finite element simulations, the pile-up behavior is well captured and matches the experimental height measurement.

### 4.4. Failure mechanisms and local stress fields

The stress field in the coating predicted by the FEM is analyzed in order to determine if a failure criterion can be identified and validated based on a maximum principal stress condition at the front of the scratch tip. Fig. 12 shows the stress component in the direction of the scratch line at the surface of the top layer. Fig. 12 has been taken at 36 µm scratch length equivalent to 7.2 mN applied load. A clear stress concentration is found both in front and behind the scratch tip.

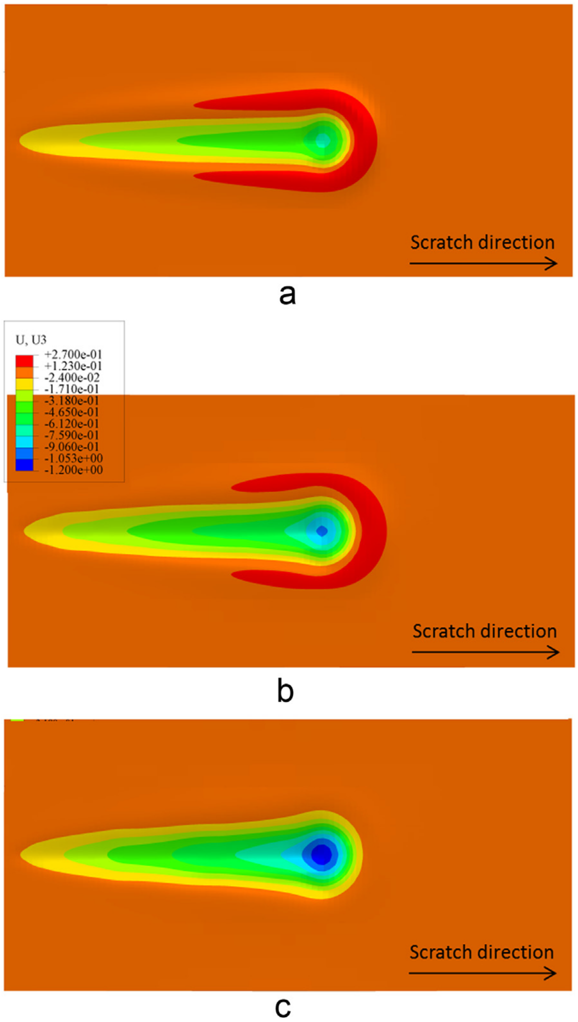


**Fig. 10.** Simulated surface displacement during scratch of the (a) 2 μm, (b) 4.5 μm and (c) 9 μm thick polyimide interlayers after 36 μm scratch under 7.2 mN applied load.

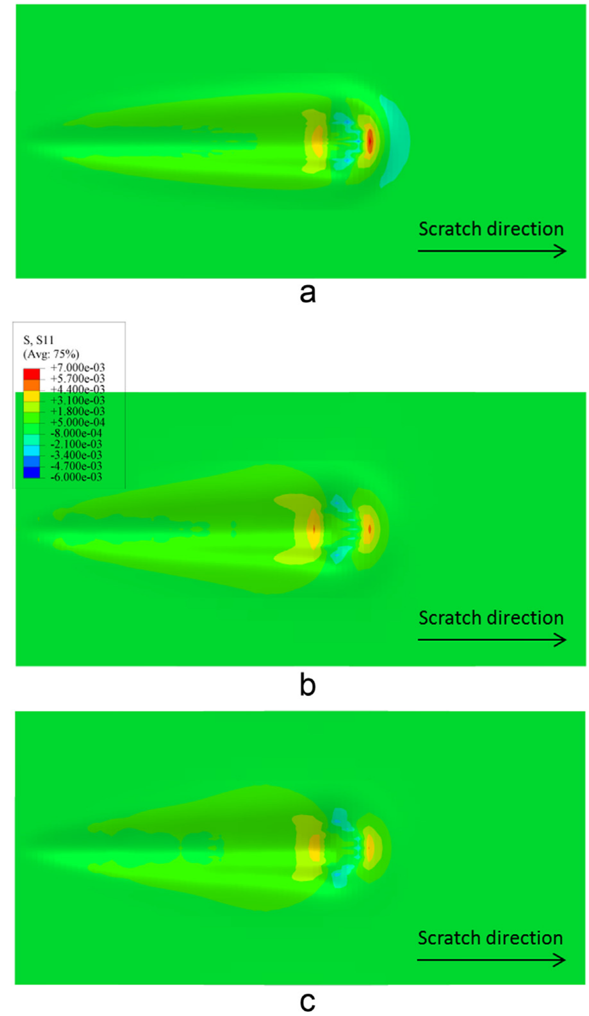


**Fig. 12.** Stress in the direction of the scratch track predicted by the FE simulations of (a) 2 μm, (b) 4.5 μm and (c) 9 μm thick polyimide interlayers after 36 μm scratch under 7.2 mN applied load.

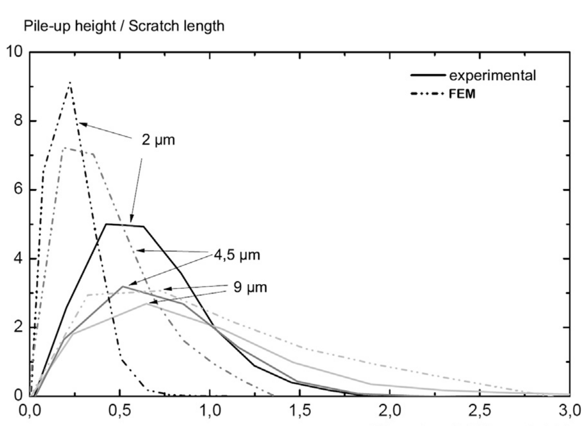


**Fig. 11.** Comparison of the normalized pile-up height as predicted by finite element simulations and measured experimentally.

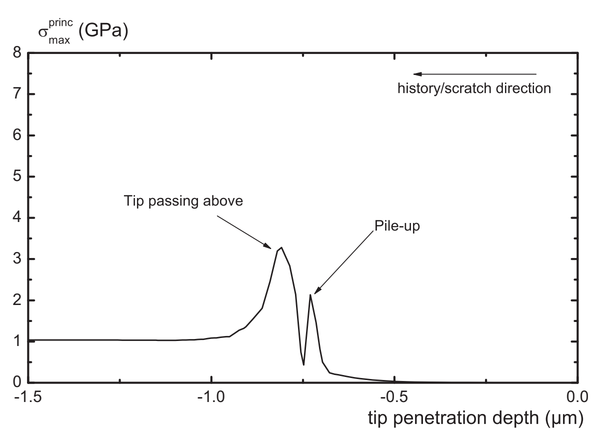


**Fig. 13.** Maximum principal stress evolution in an element located at 20 μm from the beginning of the scratch.

The maximum principal stress variation at one location as a function of the penetration depth is presented in Figs. 13 and 14 in a more quantitative way. Fig. 13 shows the maximum principal stress history of a particular element located in the middle of the scratch track at 20 μm from the scratch starting point. Fig. 13 must be read from right to left and follows the evolution of the stress history at the location of interest. From 0 to −500 nm, the stress level is zero as the material point of interest does not feel the coming tip yet. At 500 nm penetration depth, the stress level rises to a first maximum which exactly corresponds to the upper altitude of the pile-up. Afterwards, the stress level drops when the element gets located between the pile-up and the bottom of the scratch, to finally rise up again when the element is passing at the

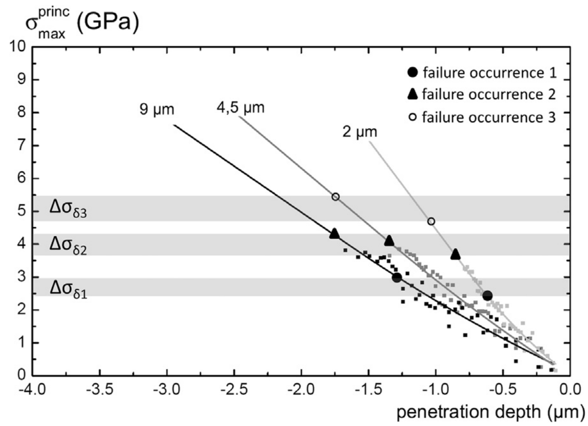


**Fig. 14.** Maximum principal stress value (under scratch loading conditions) on top of the pile-up for each element in the middle of the scratch track.

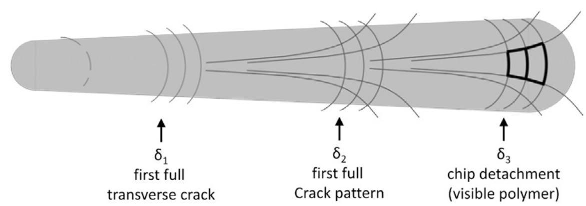


**Fig. 15.** Crack pattern scheme with definition of characteristic penetration depths $\delta_1$, $\delta_2$ and $\delta_3$.

back side of the tip. This shows that the first transverse cracks could be initiated at the back of the tip if the stress in front is not sufficient. This confirm the results of H. Jiang previously obtained on polymer coated substrates [28]. While, at larger penetration depth, corresponding to elements located further along the scratch path, cracks will preferentially be initiated at the front side.

For comparison, the maximum principal stress in the pile-up is given in Fig. 14 for the three thicknesses as the tip penetrates into the multilayer. The data have been fitted and extrapolated using a second order power law.

For a given penetration depth, the stress level in the pile-up is always higher for the lowest interlayer thickness. The lowest thickness also exhibits a faster increase of the stress level in the pile-up. This last result justifies the key role of the pile-up amplitude on the initiation of fracture. A lower polymer layer thickness leads to larger pile-up and a higher stress concentration area, leading to earlier cracking of the coating compared to a thicker interlayer.

The finite element data are compared to the experimental data to identify a value for the critical failure stress. The condition for cracking is quantified through defining three failure indicators: $\delta_1$ corresponding to the first occurrence of a full transverse cracks, $\delta_2$ corresponding to the first full array of cracks where "transverse" and "in-track" cracks are forming flakes, and $\delta_3$ corresponding to the detection of the polymer in between the flakes. The three criteria are schematically shown in Fig. 15. The scratch distance corresponding to each criterion is evaluated from SEM observation. Fig. 4 is used to determine the equivalent penetration depth. The failure occurrence corresponding to each indicator is indicated in Fig. 14 for each polymer thickness in terms of maximum principal stress in the pile-up versus penetration evolution.

Each type of failure, as quantified by $\delta_1$, $\delta_2$ and $\delta_3$, occurs in three distinct ranges of stress level. The first full transverse cracks (quantified with penetration depth $\delta_1$) appear at a distance of 60 µm for the 2 µm polymer interlayer thickness and appears at a distance of 90 µm for the 9 µm interlayer. Concerning the 4.5 µm,

**Table 3**
Experimental occurrence depth of failure and associated stress range determined by FEM.

| | 2 µm | 4.5 µm | 9 µm | $\Delta\sigma$ |
|---|---|---|---|---|
| $\delta_1$ | – 600 nm | n.a | – 1300 nm | 2.4 to 3 GPa |
| $\delta_2$ | – 800 nm | – 1300 nm | – 1750 nm | 3.7 to 4.3 GPa |
| $\delta_3$ | – 1000 nm | – 1750 nm | n.a | 4.7 to 5.5 GPa |

the first full transverse crack could not be clearly determined and no value is indicated in Fig. 14. Failure as defined by $\delta_1$ occurs at a stress value between 2.4 GPa and 3 GPa.

The same observation can be made for the two other criteria. The full crack pattern corresponding to $\delta_2$ occurs at a stress approximately ranging between 3.7 GPa and 4.3 GPa. Finally, the open pattern, with the polymer visible, corresponding to $\delta_3$, occurs under a stress ranging from 4.7 GPa to 5.5 GPa. Note that the last failure mode ($\delta_3$) for a 9 µm polymer interlayer is not attained in the range of loads applied in the scratch experiments. The results of the failure analysis are summarized in Table 3.

Assuming a 2 µm polymer interlayer, a large penetration depth involves a large pile-up. A large pile-up is the first stress concentration area seen by a section of coating and, if the stress is sufficiently large, inside the range $\Delta\sigma_{\delta_1}$, the coating breaks and forms transverse cracks. A higher pile-up will lead to more severe coating chipping. By using a thicker interlayer, the stress level to produce failure is unchanged but appears later for deeper penetration. This analysis shows that a simple maximum principal stress based criterion is sufficient to capture the key features of the scratching process by encompassing the results obtained for different interlayer thicknesses.

## 5. Conclusions

The scratch resistance of ZnO thin films deposited on a polymer interlayer has been studied through the characterization of systems with various interlayer thicknesses using nanoscratch and SEM. The support of finite element modeling has been used to determine the stress and strain fields and to identify a maximum principal stress based failure criterion.

First, the benefit on the scratch resistance of the addition of a hard nanolayer is highlighted: a 200 nm thick ZnO layer enhances the scratch resistance by 50 % in terms of load at critical failure. Second, in multilayered system with high modulus ratio, the polymer significantly affects the tip penetration and consequently the failure of the hard coating. The tip penetration increases as the polymer thickness increases and the cracking of the hard coating is delayed.

The variation of the pile-up height is found to be the root cause of the polymer thickness effect. A thinner polymer interlayer leads to higher pile-up due to the confinement of the softer material between the hard and stiff film and the hard and stiff substrate. The 3D finite element model confirms the constraint effect on the interlayer and proved that a higher pile-up is associated to larger maximum principal stress level. Several failure indicators were identified based on the SEM micrographs to quantify the scratch resistance of the coating. The simulations confirm that each type of failure occurs in the same range of stress within the pile-up validating the relevance of a maximum principal stress fracture criterion.

## Acknowledgements

The support of Inter-university Attraction Poles Program initiated by the Belgium Science Policy Office (IAP7/21) and of CRM Group is gratefully acknowledged. Computational resources have been provided by the Consortium des Equipements de Calculs Intensif (CECI), funded by the Fond de la Recherche Scientifique de Belgique (F.R.S.-FNRS) under Grant No. 2.5020.11. The work of C.-H. Sacre is supported by the Fonds de la Recherche Scientifique - FNRS under a FRIA Grant.

## References

[1] H. Chakraborty, A. Sinha, N. Mukherjee, D. Ray, P. Protim, A study on nanoindentation and tribological behaviour of multifunctional ZnO / PMMA nanocomposite, Mater. Lett. 93 (2013) 137–140.
[2] S.V. Hainsworth, P.J. Kilgallon, Temperature-variant scratch deformation response of automotive paint systems, Progress. Org. Coat. 62 (2008) 21–27.
[3] Z. Suo, Mechanics of stretchable electronics and soft machines, MRS Bull. 37 (2012) 218–225.
[4] D.-h. Kim, N. Lu, Y. Huang, J.A. Rogers, Materials for stretchable electronics in bioinspired and biointegrated devices, MRS Bull. 37 (2012) 226–235.
[5] C.-j. Chiang, C. Winscom, S. Bull, A. Monkman, Mechanical modeling of flexible OLED devices, Org. Electron. 10 (2009) 1268–1274.
[6] S. Fernandez, F.B. Naranjo, Optimization of aluminum-doped zinc oxide films deposited at low temperature by radio-frequency sputtering on flexible substrates for solar cell applications, Sol. Energy Mater. Sol. Cells 94 (2010) 157–163.
[7] J. Lewis, Material challenge for flexible organic devices, Mater. Today 9 (2006) 38–45.
[8] S. Béfahy, S. Yunus, T. Pardoen, P. Bertrand, M. Troosters, Stretchable helical gold conductor on silicone rubber microwire, Appl. Phys. Lett. 91 (2007) 1–3.
[9] P. Lacour, J. Jones, P.-h.I. Hsu, Electronic skin: architecture and components, Physica E 25 (2004) 326–334.
[10] A.A. Pelegri, X. Huang, Nanoindentation on soft film / hard substrate and hard film / soft substrate material systems with finite element analysis, Compos. Sci. Technol. 68 (2008) 147–155.
[11] D.F. Bahr, C.L. Woodcock, M. Pang, K.D. Weaver, N.R. Moody, Indentation induced film fracture in hard film / soft substrate, Int. J. Fract. 119/120 (2003) 339–349.
[12] A. Favache, C.-H. Sacré, M. Coulombier, L. Libralesso, P. Guaino, J.-P. Raskin, C. Bailly, B. Nysten, T. Pardoen, Fracture mechanics based analysis of the scratch resistance of thin brittle coatings on a soft interlayer, Wear 330–331 (2015) 461–468.
[13] T. Sander, S. Tremmel, S. Wartzack, A modified scratch test for the mechanical characterization of scratch resistance and adhesion of thin hard coatings on soft substrates, Surf. Coat. Technol. 206 (2011) 1873–1878.
[14] T.Y. Tsui, G.M. Pharr, Substrate effects on nanoindentation mechanical property measurement of soft films on hard substrates, J. Mater. Res. 14 (1999) 292–301.
[15] R. Saha, W.D. Nix, Effects of the substrate on the determination of thin film mechanical properties by nanoindentation, Acta Mater. 50 (2002) 23–38.
[16] R. Andersson, G. Toth, L. Gan, M.V. Swain, Indentation response and cracking of sub-micron silica films on a polymeric substrate, Eng. Fract. Mech. 61 (1998) 93–105.
[17] E.D. Case, C. Mukerjee, Crack spacing as a function of load for thin silica films on a polymeric substrate, Mater. Lett. 57 (2002) 302–306.
[18] K.a. Sierros, A.J. Kessman, R. Nair, N.X. Randall, D.R. Cairns, Spherical indentation and scratch durability studies of transparent conducting layers on polymer substrates, Thin Solid Films 520 (2011) 424–429.
[19] A. Favache, L. Libralesso, P.J. Jacques, J.-p. Raskin, C. Bailly, B. Nysten, T. Pardoen, Fracture toughness measurement of ultra-thin hard fi lms deposited on a polymer interlayer, Thin Solid Films 550 (2014) 464–471.
[20] S. Bull, Failure modes in scratch adhesion testing, Surf. Coat. Technol. 50 (1991) 25–32.
[21] F.W. Zok, A. Miserez, Property maps for abrasion resistance of materials, Acta Mater. 55 (2007) 6365–6371.
[22] F. Wredenberg, P.-L. Larsson, On the numerics and correlation of scratch testing, J. Mech. Mater. Struct. 2 (2007) 573–594.
[23] S. Bellemare, M. Dao, S. Suresh, Effects of mechanical properties and surface friction on elasto-plastic sliding contact, Mech. Mater. 40 (2008) 206–219.
[24] S.E. Flores, M.G. Pontin, F.W. Zok, Scratching of elastic / plastic materials with hard spherical indenters, J. Appl. Mech. 75 (2008) 1–7.
[25] E. Felder, J.-l. Bucaille, Mechanical analysis of the scratching of metals and polymers with conical indenters at moderate and large strains, Tribology Int. 39 (2006) 70–87.
[26] J.-l. Bucaille, C. Gauthier, E. Felder, R. Schirrer, The influence of strain hardening of polymers on the piling-up phenomenon in scratch tests: experiments and numerical modelling, Wear 260 (2006) 803–814.
[27] K. Holmberg, A. Laukkanen, H. Ronkainen, K. Wallin, S. Varjus, A model for stresses, crack generation and fracture toughness calculation in scratched TiN-coated steel surfaces, Wear 254 (2003) 278–291.
[28] H. Jiang, R. Browning, J.D. Whitcomb, M. Ito, M. Shimouse, T.A. Chang, H.J. Sue, Mechanical modeling of scratch behavior of polymeric coatings on hard and soft substrates, Tribology Lett. 37 (2010) 159–167.
[29] P. Chouwatat, M. Kotaki, M. Miyamoto, R. Nishimura, A. Yokohama, Effect of soft base layer on scratch properties of acrylic hard coatings, Polym. Eng. Sci. 56 (2016) 528–535.
[30] A. Moezzi, A.M. Mcdonagh, M.B. Cortie, Zinc oxide particles: synthesis, properties and applications, Chem. Eng. J. 185–186 (2012) 1–22.
[31] M. Berginski, J. Hüpkes, W. Reetz, B. Rech, M. Wuttig, Recent development on surface-textured ZnO: Al films prepared by sputtering for thin-film solar cell application, Thin Solid Films 516 (2008) 5836–5841.
[32] Z. Chen, L.Y.L. Wu, E. Chwa, O. Tham, Scratch resistance of brittle thin films on compliant substrates, Mater. Sci. Eng. A 493 (2008) 292–298.
[33] W. Gao, Z. Li, ZnO thin films produced by magnetron sputtering, Ceram. Int. 30 (2004) 1155–1159.
[34] V. Tvarozek, I. Novotny, P. Sutta, S. Flickyngerova, K. Schtereva, E. Vavrinsky, Influence of sputtering parameters on crystalline structure of ZnO thin films, Thin Solid Films 515 (2007) 8756–8760.
[35] W.C. Oliver, G. Pharr, An improved technique for determining hardness and elastic modulus using load and displacement sensing indentation experiments, J. Mater. Res. 7 (1992) 1564–1583.
[36] P.-f. Yang, H.-c. Wen, S.-r. Jian, Y.-s. Lai, S. Wu, R.-s. Chen, Characteristics of ZnO thin films prepared by radio frequency magnetron sputtering 48 (2008) pp. 389–394.
[37] J.B. Pethica, D. Tabor, Contact of characterised metal surfaces at very low loads: deformation and adhesion, Surf. Sci. 89 (1979) 182–190.
[38] ⟨http://www.dupont.com/content/dam/dupont/products-and-services/membranes-and-films/polyimde-films/documents/DEC-Kapton-summary-of⟩ properties.pdf, Summary of properties for kapton polyimide films, last accessed, 11-2016.